Article

Microstructure of Laser Re-Melted AlCoCrCuFeNi High Entropy Alloy Coatings Produced by Plasma Spraying

Tai M. Yue [1,*], Hui Xie [1,†], Xin Lin [2], Haiou Yang [2] and Guanghui Meng [1]

[1] Advanced Manufacturing Technology Research Centre, Department of Industrial and Systems Engineering, Hong Kong Polytechnic University, Hung Hom, Kowloon, Hong Kong; E-Mails: xaxiehui@163.com (H.X.); mghxu@hotmail.com (G.M.)

[2] State Key Laboratory of Solidification Processing, Northwestern Polytechnical University, Xi'an 710072, China; E-Mail: xlin@nwpu.edu.cn (X.L.); yanghaiou@hotmail.com (H.Y.)

[†] Current address: School of Mechanical Engineering, Xi'an Aeronautical University, Xi'an 710077, China.

[*] Author to whom correspondence should be addressed; E-Mail: tm.yue@polyu.edu.hk; Tel.: +852-2766-6601; Fax: +852-2362-5267.

Abstract: An AlCoCrCuFeNi high-entropy alloy (HEA) coating was fabricated on a pure magnesium substrate using a two-step method, involving plasma spray processing and laser re-melting. After laser re-melting, the microporosity present in the as-sprayed coating was eliminated, and a dense surface layer was obtained. The microstructure of the laser-remelted layer exhibits an epitaxial growth of columnar dendrites, which originate from the crystals of the spray coating. The presence of a continuous epitaxial growth of columnar HEA dendrites in the laser re-melted layer was analyzed based on the critical stability condition of a planar interface. The solidification of a columnar dendrite structure of the HEA alloy in the laser-remelted layer was analyzed based on the Kurz–Giovanola–Trivedi model and Hunt's criterion, with modifications for a multi-component alloy.

1. Introduction

In recent years, much interest has been generated in applying magnesium alloys for stress-bearing applications in the automotive and aerospace industries [1,2]. Unfortunately, magnesium is high in the electrochemical series, so the metal is highly susceptible to galvanic corrosion when contact is made with other metals. Moreover, metallic impurities in magnesium alloys can cause severe pitting corrosion when exposed to moist conditions, especially in the presence of chloride ions. To combat the problem of corrosion in magnesium alloys, many protective coating techniques have been developed. Gray and Luan [3] have written an excellent review paper on this subject. It is generally accepted that it is necessary to apply a surface protective coating to magnesium components or products if they are to survive in a harsh working environment. Indeed, over the years, intensive research efforts have been devoted to developing better coatings for combating the poor corrosion and wear properties of magnesium alloys in order to meet the challenges demanded by industry. Studies conducted by the authors [4–6] and other researchers [7–10] have already shown that laser cladding can be used to improve the corrosion and wear resistance of magnesium alloys.

Notwithstanding that protective coatings can be fabricated on Mg alloys using laser surface processing techniques [11], the main problems of the high chemical reactivity, the relatively low melting and boiling points of Mg alloys, and the formation of brittle intermetallic compounds in the coating cannot be easily overcome. Another common problem encountered in the laser cladding of a protective coating on Mg substrates is that significant dilution from the substrate often occurs, and this can adversely affect the corrosion resistance of the coating. Recognizing these problems, this research has adopted a two-step approach, which involves plasma spraying a high-entropy alloy (HEA) coating on the Mg substrate first, and then re-melting this coating using a laser, to circumvent the inherent problems. Such a technique can avoid excessive melting and boiling of the Mg substrate, and it has been successfully employed to deposit stainless steel and pure zirconium on Mg [12,13].

HEAs are based on a new alloy design concept—multi-principal elements—made up of more than five metallic elements in equimolar or near-equimolar ratios, explored and developed by Yeh *et al.* [14,15]. These alloys are unique in that they have simple solid solution structures, essentially bcc and/or fcc phases, with or without nano-precipitation; moreover, they exhibit good wear resistance, excellent corrosion resistance, excellent oxidation resistance, low electrical conductivity, low thermal conductivity and a low coefficient of thermal expansion. So far, most of the studies on HEAs have been concerned with the microstructure and properties of the cast materials and only a limited number of studies have focused on their usage in surface modification [16–18]. This study focuses on the study of the microstructure of the laser re-melted HEA coatings produced by plasma spraying.

2. Experimental Details

The two-step technique involved plasma spraying a HEA coating on the pure (99.9 wt%) Mg substrate first, and then using laser re-melting to densify the coating. Using plasma spraying can avoid excessive melting and boiling of the Mg substrate; while laser re-melting is required to increase the coating density because normally it is difficult to obtain a fully dense coating using plasma spraying alone. In this

study, pure Mg instead of Mg alloys, such as AZ91, was used, the reason is to avoid any complications associated with the dilution of the HEA by the alloying elements of the substrate material, if any.

The AlCoCrCuFeNi HEA powder with a mesh size of 200–300 used in the experiment was prepared by the Central South University in China, by means of argon gas atomization of the HEA melt, which was produced using elemental metals (Al 99.8%, Ni 99.95%, Co 99.95%, Cr 99.8%, Cu 99.9% and Fe 99.9%). The HEA powder was dried using a vacuum oven for 24 hours prior to the experiment. For the spraying of HEA on the Mg substrate, a low-velocity air plasma spray system developed by researchers at Xi'an Jiaotong University was employed [19]. It was designed to provide a uniform heating effect on the metal powder with high deposition efficiency. In the experiment, forty passes were applied in the spraying process. The plasma spray parameters used are given in Table 1. After the deposition of an HEA coating by spraying, laser re-melting, using a 300 W Nd:YAG pulsed laser (Model WF300, Han's Laser, Shenzhen, China), was employed to obtain a dense surface coating. Laser processing was conducted inside a controlled-atmosphere glove box, where high-purity argon gas was continuously supplied at a flow rate of 10 litres per minute to prevent the molten metal from oxidizing. In the experiment, the pulse energy and the frequency were set at 240 J and 6 Hz, respectively. The laser beam size was fixed at 1 mm, with scanning speed of 2 mm/s, and a 30% multi-track overlap condition was used.

Table 1. Plasma spray parameters.

Plasma gas	Ar/H$_2$
Primary gas flow, Ar (L/min)	90
Second gas flow (L/min)	5
Arc voltage (V)	110
Arc current (A)	330
Powder feeding rate (g/min)	30
Spray distance (mm)	100

The phase and crystal structures of the as-sprayed and the laser-remelted HEA coatings were analyzed using the X-ray diffraction (XRD) technique with a Rigaku SmartLab X-ray diffractometer (Rigaku Corporation, Tokyo, Japan) using Cu-K α radiation at 40 kV and 30 mA. The specimens for microscopic study were ground with a series of emery papers and finally polished with 1 μm diamond abrasives. To reveal the microstructure, the HEA coating was etched in the regent of aqua regia, and the microstructure was studied using a JEOL JSM-6490 (JEOL Ltd., Tokyo, Japan) scanning electron microscope equipped with energy dispersive x-ray spectroscopy (EDX). The porosity levels of the coatings were measured using a Leica DM4000M optical microscope (Leica Microsystems, Wetzlar, Germany) equipped with an image analyzer software.

3. Results and Discussion

3.1. Microstructure and Epitaxial Growth

Figure 1 shows a cross-section of the HEA coating deposited on the Mg substrate, which comprises a lower plasma-sprayed layer and an upper laser-remelted layer, with a total coating thickness of

about 275 μm. The as-sprayed layer consists of flattened lamellae (Figure 2) with the presence of some micro-porosity (Figure 3), which are typical features resulting from plasma spray methods. The average porosity level measured for the sprayed coating was 10%. Lying above the sprayed layer is a compact laser-remelted layer, in which only very few isolated small pores can be found (Figure 1); the coating is virtually free of porosity.

Figure 1. A transverse section of an HEA coated Mg specimen, showing the lower plasma-sprayed layer and the upper laser-remelted layer (unetched), in the latter, a pore was found (indicated by the arrow).
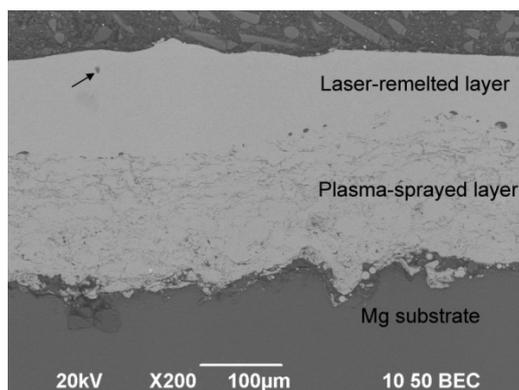

Figure 2. The flattened lamellae structure of the as-sprayed layer (unetched).
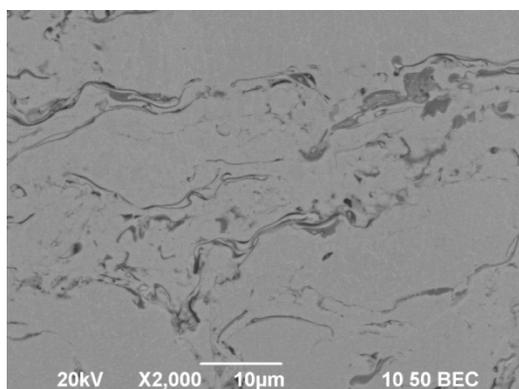

Figure 3. A higher magnification of Figure 1, showing the epitaxial growth of columnar dendrites at the re-melted boundary of the plasma-sprayed layer; micro-porosity is present in the plasma-sprayed layer.
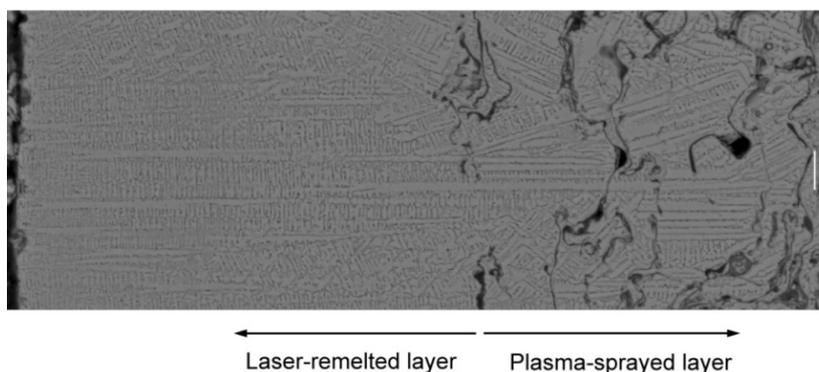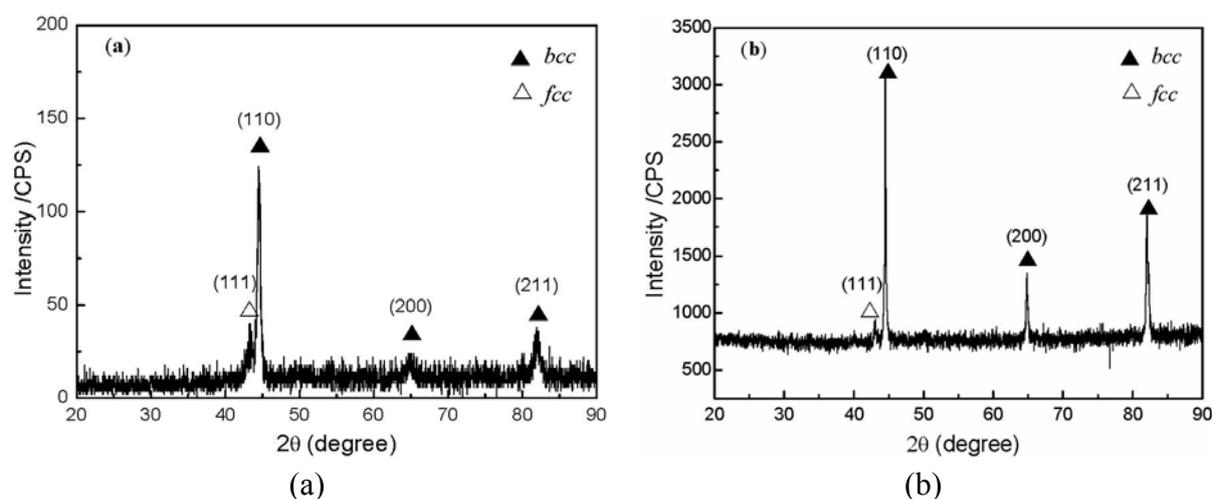
Figure 4 shows the XRD patterns of the as-sprayed HEA and the laser-remelted HEA coatings. These two patterns revealed that there was no significant difference between the phases of these two types of coatings. They are composed primarily of a bcc solid solution phase with a small amount of fcc phase. There is no sign of the presence of intermetallic compounds. Moreover, the XRD analysis did not show any oxides in the laser-remelted coating, revealing that effective protection against oxidation was obtained during laser remelting. The formation of simple solid solutions was due to the effect of the high mixing entropy. According to Boltzmann's hypothesis, the high mixing entropy of solid solutions with multi-principal elements lowers the tendency to ordering and segregation [14,15]. For the experimental multi-element alloy (AlCoCrCuFeNi), its mixing entropy has a maximum at an equi-atomic ratio. Thus, the AlCoCrCuFeNi multi-element alloy solidifies to form solid solutions rather than intermetallics or ordered phases.

Figure 4. XRD patterns of (**a**) the plasma-sprayed coating, and (**b**) the laser re-melted layer.

(a)   (b)

The microstructure of the laser-remelted layer consists of columnar dendrites of a bcc structure and an interdendritic fcc phase, in which porosity was not observed. The EDX results of the compositions of the dendrite and the interdendritic phases are given in Table 2, which indicate that there was a segregation of Cu in the interdendritic regions. The study of Cu being rejected to interdendritic regions during solidification will be reported in a separate paper. An epitaxial growth of columnar dendrites was observed at the re-melted boundary of the plasma-sprayed layer, growing along the temperature gradient direction. This is different from the planar growth that is often obtained at the re-melted boundary of the substrate in the laser melting and laser cladding of metal alloys [20]. In this study, the columnar dendrites solidified in a directional manner, as the crystals grew in an upward direction, and gas bubbles more readily escaped due to the buoyancy effect [21]. This together with the high cooling rates in laser re-melting favor a porosity free structure because a high cooling decreases the amount of porosity [22].

Table 2. EDX results of the dendritic and the interdendritic regions (at%).

	Al	**Cr**	**Fe**	**Co**	**Ni**	**Cu**
Dendrite	11.50	18.96	19.22	19.68	19.06	11.56
Interdendritic	12.94	17.31	18.05	19.04	17.51	15.14

In order to examine the conditions under which epitaxial growth of the AlCoCrCuFeNi HEA occurred, an analysis of the planar interface stability in laser re-melting was conducted based on the analytical model developed by Hunziker [23], *i.e.*, the critical stability of a planar interface, which is governed by the following equation:

$$\frac{\dot{\delta}}{\delta} = \frac{V\omega(K_S + K_L)}{K_S G_S - K_L G_L}(\sum_{i=1}^{n}(m_i \sum_{j=1}^{n}(-V\frac{A_{ij}}{B_j} + E_{ij})) - \Gamma\omega^2 - \frac{K_S G_S + K_L G_L}{K_S + K_L})$$ (1)

where $\dot{\delta}$ is the time derivative of the perturbation (instability) amplitude δ, Γ is the Gibbs-Thomson coefficient, $\omega = 2\pi/\lambda$ is the wave-number, λ is the perturbation wavelength, K_S and K_L are the thermal conductivities of the solid and liquid respectively, G_S is the temperature gradient in the solid. The coefficients B_j are the n eigenvalues of the diffusion matrix, V is the solidification velocity, A_{ij} *is* the ith component of the eigenvector A_j corresponding to the eigenvalue B_j, and E_{ij} *is* the component of the eigenvector E_j of the diffusion matrix.

Given that the first term on the right-hand side of Equation (1) is always positive, the critical stability condition can be presented as:

$$\sum_{i=1}^{n}(m_i \sum_{j=1}^{n}(-V\frac{A_{ij}}{B_j} + E_{ij})) - \Gamma\omega^2 - \frac{K_S G_S + K_L G_L}{K_S + K_L} = 0$$ (2)

However, solute diffusion in liquid metals is very difficult to measure, and very little data can be found in the literature. Therefore, the diffusional interaction was not included in the analysis. For a multi-component high entropy alloy, Equation (1) can be rewritten as:

$$\frac{\dot{\delta}}{\delta} = \frac{V\omega(\sum_{i=1}^{n-1}m_i G_{Ci}^P \xi_{Ci}^P - \Gamma\omega^2 - (K_S G_S + K_L G_L)/(K_S + K_L))}{(K_S G_S - K_L G_L)/(K_S + K_L) + \sum_{i=1}^{n-1}(m_i G_{Ci}\omega/(\omega_i^* - (V/D_i)(1-k_i)))}$$ (3)

where:

$$G_{Ci}^P = -\frac{VC_{0i}(1-k_i)}{D_i}$$ (4)

$$\xi_{Ci}^P = 1 - \frac{2k_i}{[1 + (2\omega D_i/V)^2]^{1/2} - 1 + 2k_i}$$ (5)

$$\omega_i^* = \frac{V}{2D_i} + \left[\left(\frac{V}{2D_i}\right)^2 + \omega^2\right]^{1/2}$$ (6)

G_{ci}^p is the solute concentration gradient of component i in the liquid at the unperturbed interface, C_{0i} is the nominal concentration of component i, D_i is the diffusion coefficient of the solute in the liquid of component i, and k_i is the equilibrium partition coefficient.

Now, the critical stability condition can be expressed as:

$$\sum_{i=1}^{n}m_i G_{Ci}^P \xi_{Ci}^P - \Gamma\omega^2 - \frac{K_S G_S + K_L G_L}{K_S + K_L} = 0$$ (7)

The critical perturbation wavelength for the instability of a planar interface can be obtained by solving Equation (7). On the other hand, according to Kurz's analysis [24], the primary dendrite arm spacing (λ_1) for a given growth velocity can be expressed as a function of the dendrite tip radius, thus:

$$\lambda_1 = \sqrt{\frac{3 \Delta T R}{G_L}} \tag{8}$$

where $\Delta T'$ is the non-equilibrium solidification range (for the HEA in this study, ΔT is 160 K), and G_L is the temperature gradient of the liquid for columnar dendrite growth.

Based on the above analysis, the predicted critical perturbation wavelength (λ_C), the fastest growth perturbation wavelength (λ_F), and the primary dendrite arm spacing (λ_1) as a function of the solidification velocity for the AlCoCrCuFeNi multi-element alloy were obtained (Figure 5). In the analysis, G_L was set at 3×10^6 K/m which is a typical value for the laser surface melting process [25,26]. Other physical parameters used for the analysis are given in Table 3. The primary dendrite arm spacing of the microstructure of the laser-remelted HEA coating was measured as being in the range of 2–2.5 μm, and this is indicated in Figure 5. The results of the analysis showed that the dimensions of both the measured primary arm spacing and the initial fastest growth perturbation wavelength are very close to each other, and fall within the zone where planar growth becomes unstable. In the plasma-sprayed layer, the columnar crystals at the re-melted boundary are favourable sites for the development of perturbations. In fact, the solute atoms rejected to the perturbation front would suppress the development of a planar interface. As a result, perturbations will grow with a similar morphology as the underlying crystals, and according to the results of the analysis, continued epitaxial dendrite growth of columnar HEA crystals would occur. This agrees with the microstructure observed at the laser re-melted boundary.

Figure 5. The predicted critical perturbation wavelength (λ_C), the perturbation wavelength (λ_F) with a maximum amplification rate, and the predicted primary dendrite arm spacing (λ_1) for the AlCoCrCuFeNi HEA under the condition of a thermal gradient of 3.0×10^6 K/m. The shaded zone represents the measured dendrite arm spacing range; the vertical dotted line represents the maximum solidification velocity of 2 mm/s.
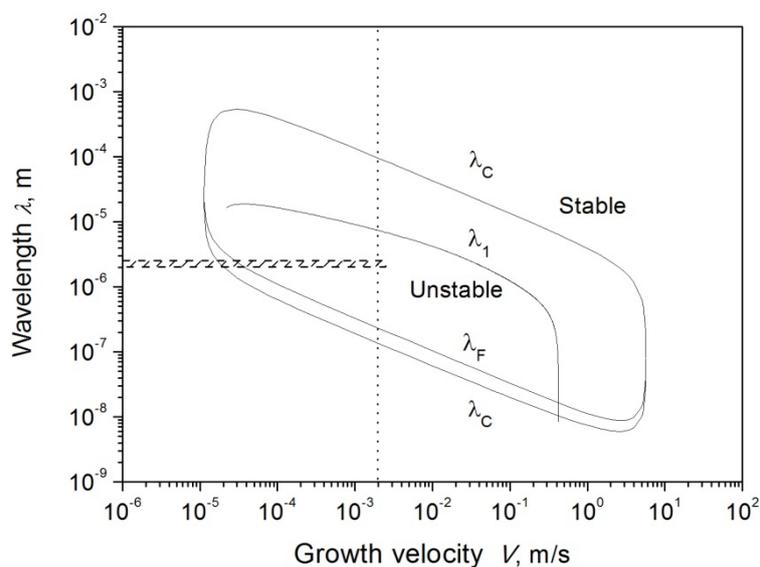
Table 3. Physical parameters of the AlCoCrCuFeNi multi-element alloy used for calculating the results of Figures 5 and 6 [27].

Liquidus temperature of AlCoCrCuFeNi, T_L	1501.17 K *
Gibbs-Thomson coefficient, Γ	2.47×10^{-7} K m
Linear kinetic coefficient, μ_k	4.696 m/s K
Length scale for solute trapping, a_0	5×10^{-9} m
Latent heat, ΔH	4.3992×10^4 J mol^{-1}
Concentration of chromium, C_{0Cr}	16.67 at%
Concentration of cobalt, C_{0Co}	16.67 at%
Concentration of iron, C_{0Fe}	16.67 at%
Concentration of aluminum, C_{0Al}	16.67 at%
Concentration of copper, C_{0Cu}	16.67 at%
Partition coefficient for chromium, k_{Cr}	0.237 *
Partition coefficient for cobalt, k_{Co}	1.148 *
Partition coefficient for iron, k_{Fe}	0.512 *
Partition coefficient for aluminum, k_{Al}	2.02 *
Partition coefficient for copper, k_{Cu}	0.399
Slope of liquidus surface with respect to aluminum concentration, m_{Al}	15.36 K/at% *
Slope of liquidus surface with respect to cobalt concentration, m_{Co}	−1.039 K/at% *
Slope of liquidus surface with respect to chromium concentration, m_{Cr}	−2.625 K/at% *
Slope of liquidus surface with respect to iron concentration, m_{Fe}	−3.175 K/at% *
Slope of liquidus surface with respect to copper concentration, m_{Cu}	−3.974 K/at% *
Pre-exponential diffusion coefficient for aluminum, D_{Al}^0	1.53×10^{-7} m^2/s
Pre-exponential diffusion coefficient for cobalt, D_{Co}^0	2.30×10^{-7} m^2/s
Pre-exponential diffusion coefficient for chromium, D_{Cr}^0	2.22×10^{-7} m^2/s
Pre-exponential diffusion coefficient for iron, D_{Fe}^0	2.29×10^{-7} m^2/s
Pre-exponential diffusion coefficient for copper, D_{Cu}^0	2.15×10^{-7} m^2/s
Activation energy for Al diffusion, Q_{Al}	4.7893×10^{-4} J/mol
Activation energy for Co diffusion, Q_{Co}	6.5314×10^{-4} J/mol
Activation energy for Cr diffusion, Q_{Cr}	6.6466×10^{-4} J/mol
Activation energy for Cu diffusion, Q_{Cu}	6.0630×10^{-4} J/mol
Activation energy for Fe diffusion, Q_{Fe}	6.5515×10^{-4} J/mol
Thermal diffusion coefficient, a	3.89×10^{-6} m^2/s

* obtained using Thermo-Calc Software-CALPHAD.

3.2. Columnar to Equiaxed Transition

It is understood that in laser surface melting, the solidification velocity will increase gradually as the distance increases from the bottom of the melt pool, and this is accompanied with a decrease in temperature gradient. Accordingly, the solidification velocity will reach a maximum at the top surface of the melt pool and it will be close to the laser scanning velocity. Under such a condition, a columnar to equiaxed transition (CET) of crystal growth is often found in laser melting and laser cladding, especially towards the final stage of the solidification process [28]. However, such a phenomenon was not observed in the laser re-melted layer (Figure 3). To the best knowledge of the authors, the CET phenomenon in multi-element HEAs has not been studied previously. Recognizing this, the following

presents an analysis of CET for the AlCoCrCuFeNi HEA under a laser re-melting condition. The analysis was based on the Kurz–Giovanola–Trivedi (KGT) model [29] and Hunt's criterion [30], *i.e.*, a columnar crystal growth is maintained when the volume fraction of the equiaxed crystals is below 0.66%. In fact, CET is closely related to both the undercooling and the volume fraction of equiaxed crystals at the liquid-solid interface. According to the KGT model, the dendrite tip undercooling ΔT can be expressed as:

$$\Delta T = \Delta T_c + \Delta T_r + \Delta T_k \tag{9}$$

The three terms on the right-hand side of Equation (9) represent the chemical undercooling, the curvature undercooling, and the kinetic undercooling, respectively. For a multi-element alloy, Equation (9) can be rewritten according to Gäumann's model [31], which is a modification resulting from combining the KGT model for directional solidification and the Lipton-Kurz-Trivedi model (LKT) model [32] for an undercooled melt growth, *i.e.*:

$$\Delta T = \sum_{i=1}^{n-1} m_{Vi} C_i^* - \frac{2\Gamma}{R} - \frac{V}{\mu_k} \tag{10}$$

where μ_k is the linear kinetic coefficient, V is the solidification velocity, and the relationships between other parameters in Equation (10) are given by the following equations:

$$R = \left[\frac{\Gamma/\sigma^*}{\sum_{i=1}^{n-1} m_{Vi} G_{Ci} \xi_{Ci}(Pe_i) - G_T} \right]^{1/2} \tag{11}$$

$$G_{Ci} = -\frac{V C_i^*(1 - k_{Vi})}{D_i} \tag{12}$$

$$m_{Vi} = m_i \left\{ 1 + \frac{k_i - k_{Vi}[1 - \ln(k_{Vi}/k_i)]}{1 - k_i} \right\} \tag{13}$$

$$\xi_C(Pe_i) = 1 - \frac{2k_{Vi}}{[1 + 1/(\sigma^* Pe_i^2)]^{1/2} - 1 + 2k_{Vi}} \tag{14}$$

$$Pe_i = \frac{VR}{2D_i} \tag{15}$$

$$k_{Vi} = \frac{k_i + a_0 V/D_i}{1 + a_0 V/D_i} \tag{16}$$

$$C_i^* = \frac{C_{0i}}{1 - (1 - k_{Vi})Iv(Pe_i)} \tag{17}$$

where m_{Vi} is the velocity dependent liquidus slope of component i, G_{Ci} is the concentration gradient of component i in the liquid at the dendrite tip, ξ_C is the stability parameter, Pe_i is the solute Peclet number for component i, σ^* is a given constant of $\frac{1}{4\pi^2}$, C_i^* is the composition of the liquid at the dendrite tip, k_{Vi} is the velocity dependent partition coefficient of component i, m_i is the liquidus slope

of component i, a_0 is the characteristic length in the order of an atomic distance, C_{0i} is the nominal concentration of component i, Iv is the Ivantsov function $Iv(Pe_i) = Pe_i \exp(Pe_i) E_1(Pe_i)$, where E_1 is the exponential integral function, and G_T is the effective temperature gradient ($G_T = G_L$ for columnar dendrite growth, whereas $G_T = G_L/2$ for equiaxed growth). The degree of constitutional undercooling ahead of the solidification interface, ΔT, and the dendritic tip radius can be determined as a function of the solidification velocity (V) and the temperature gradient (G_T) by solving Equations (9)–(17).

Although the nucleation of equiaxed crystals can occur if ΔT ahead of the solid-liquid interface is greater than the nucleation undercooling of the equiaxed crystals, the leading condition for CET to occur is controlled by the volume fraction of equiaxed crystals in the liquid more than the nucleation undercooling. The actual volume fraction   of the equiaxed crystals formed can be obtained by using the Avrami Equation [33]:
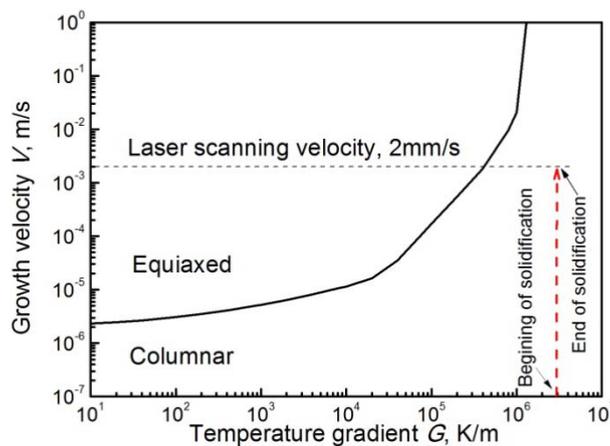
$$\phi = 1 - \exp[-\phi_e] \tag{18}$$

$$\phi_e = \frac{4}{3} \pi r_e^3 N_0 \tag{19}$$

$$r_e = \int_0^{z_n} \frac{V_e[z]}{V} dz \tag{20}$$

where $_e$ is the extended volume fraction, r_e is the maximum radius of the equiaxed crystals, N_0 is the total number of heterogeneous nucleation sites per unit volume, Z_n is the distance from the interface of the undercooled liquid, and ΔT_n is the nucleation undercooling. For equiaxed crystal growth, the constitutional undercooling ahead of the interface and the growth velocity V_e can be obtained by solving Equations (9)–(17). Using Hunt's criterion [30] for columnar growth, *i.e.*, the equiaxed crystal volume is below 0.66 pct, the critical solidification velocity and temperature gradient required for CET to occur in laser re-melting of the HEA coating were obtained and the results are presented in Figure 6.

Figure 6. The CET curve of the AlCrFeCoNi HEA, showing the solidification conditions for the growth of columnar crystals and equiaxed crystals.

The physical parameters used for the analysis are given in Table 3. The results show that the crystal growth velocity increases rapidly at the bottom of the melt pool to a value close to the laser scanning velocity at the top of the melt pool, *i.e.*, 2 mm/s (shown by the dotted arrow line). In the analysis, a thermal gradient of 3.0×10^6 K/m was used; this is a reasonable assumption, for this value has been

predicted for the laser surface melting process [25,26]. The results show that columnar crystal growth will dominate the entire solidification process and CET would not occur. This tallies with the columnar microstructure that was observed in the laser re-melted layer (Figure 3). From the kinetics viewpoint, the absence of CET is considered to be due to the sluggish diffusion kinetics of the HEAs [14,15], which leads to a reduction of the degree of undercooling at the solid-liquid interface and the extent of the undercooled liquid zone. As a result, the CET phenomenon is suppressed, and the growth of columnar crystals becomes dominant in the laser re-melted layer.

4. Conclusions

A two-step method utilizing plasma spraying and laser surface melting has been used to fabricate a high entropy alloy (HEA) coating, having an equi-atomic AlCoCrCuFeNi ratio, on a Mg substrate. The as-sprayed HEA coating was found to contain micro-porosity with sizes on the order of 50 μm; after laser re-melting, no apparent porosity was observed in the re-solidified layer. The XRD results showed that both the as-sprayed and the laser-remelted coatings are composed primarily of a bcc solid solution phase with a small amount of fcc phase, and no intermetallic compounds were found.

An epitaxial growth of columnar dendrites was observed at the re-melted boundary of the plasma-sprayed layer and they grew along the temperature gradient direction towards the top of the coating. The epitaxial growth of HEA crystals can be predicted using the critical stability condition of a planar interface. Moreover, the relationship between the critical perturbation wavelength, the fastest growth perturbation wavelength, the primary dendrite arm spacing and the solidification velocity for the AlCoCrCuFeNi multi-element alloy was established. The predominant growth of columnar crystals in the laser-remelted layer was confirmed by a CET analysis based on Hunt's criterion. The absence of the CET phenomenon is believed to be due to the sluggish diffusion kinetics of the HEAs.

Acknowledgments

Conflict of Interest

The authors declare no conflict of interest.

References

1. Cole, G.S. Summary of "Magnesium vision 2020: A North American automotive strategic vision for magnesium". In *Magnesium Technology 2007*, Proceedings of the Symposium on Magnesium Technology, TMS Annual Meeting and Exhibition, Orlando, FL, USA, 25 February–1 March 2007; Beals, R.S., Luo, A.A., Neelameggham, N.R., Pekguleryuz, M.O., Eds.; Minerals, Metals & Materials Society: Warrendale, PA, USA, 2007; pp. 35–40.

2. Dieringa, H.; Bohlen, J.; Hort, N.; Letzig, D.; Kainer, K.U. Advances in manufacturing processes for magnesium alloys. In *Magnesium Technology 2007*, Proceedings of the Symposium on Magnesium Technology, TMS Annual Meeting and Exhibition, Orlando, FL, USA, 25 February–1 March 2007; Beals, R.S., Luo, A.A., Neelameggham, N.R., Pekguleryuz, M.O., Eds.; Minerals, Metals & Materials Society: Warrendale, PA, USA, 2007; pp. 3–8.

3. Gray, J.E.; Luan, B. Protective coatings on magnesium and its alloys—a critical review. *J. Alloys Compd.* **2002**, *336*, 88–113.

4. Yue, T.M.; Su, Y.P. Laser multi-layer cladding of $Zr_{65}Al_{7.5}Ni_{10}Cu_{17.5}$ amorphous alloy on magnesium substrates. *J. Mater. Sci.* **2007**, *42*, 6153–6160.

5. Yue, T.M.; Li, T. Laser cladding of Ni/Cu/Al functionally graded coating on magnesium substrate. *Surf. Coat. Technol.* **2008**, *202*, 3043–3049.

6. Yue, T.M.; Li, T.; Lin, X. Microstructure and phase evolution in laser cladding of Ni/Cu/Al multilayer on magnesium substrates. *Metall. Mater. Trans. A* **2010**, *41*, 212–223.

7. Subramanian, R.; Sircar, S.; Mazumder, J. Laser cladding of zirconium on magnesium for improved corrosion properties. *J. Mater. Sci.* **1991**, *26*, 951–956.

8. Wang, A.A.; Sircar, S.; Mazumder, J. Laser cladding of Mg-Al alloys. *J. Mater. Sci.* **1993**, *28*, 5113–5122.

9. Maiwald, T.; Galun, R.; Mordike, B.L.; Feikus, F.J. Microstructure and corrosion properties of laser clads of magnesium base alloys for laser generated cylinder liners. *Lasers Eng.* **2002**, *12*, 227–238.

10. Volovitch, P.; Masse, J.E.; Fabre, A.; Barrallier, L.; Saikaly, W. Microstructure and corrosion resistance of magnesium alloy ZE41 with laser surface cladding by Al-Si powder. *Surf. Coat. Technol.* **2008**, *202*, 4901–4914.

11. Singh, A.; Harimkar, S.P. Laser surface engineering of magnesium alloys: A review. *JOM* **2012**, *64*, 716–733.

12. Yue, T.M.; Hu, Q.W.; Mei, Z.; Man, H.C. Laser cladding of stainless steel on magnesium ZK60/SiC composite. *Mater. Lett.* **2001**, *47*, 165–170.

13. Yue, T.M.; Xie, H.; Lin, X.; Yang, H.O. Eutectic growth in laser cladding of Zr-coating on AZ91D magnesium substrate. *Mater. Trans.* **2012**, *53*, 1119–1123.

14. Yeh, J.W.; Chen, S.K.; Lin, S.J.; Gan, J.Y.; Chin, T.S.; Shun, T.T.; Tsau, C.H.; Chang, S.Y. Nanostructured high-entropy alloys with multiple principal elements: Novel alloy design concepts and outcomes. *Adv. Eng. Mater.* **2004**, *6*, 299–303.

15. Yeh, J.W. Recent progress in high-entropy alloys. *Ann. Chim.-Sci. Mat.* **2006**, *31*, 633–648.

16. Li, Q.H.; Yue, T.M.; Guo, Z.N.; Lin, X. Microstructure and corrosion properties of AlCoCrFeNi high entropy alloy coatings deposited on AISI 1045 Steel by the electrospark process. *Metall. Mater. Trans. A* **2013**, *44*, 1767–1778.

17. Qiu, X.W.; Liu, C.G. Microstructure and properties of $Al_2CrFeCoCuTiNi_x$ high-entropy alloys prepared by laser cladding. *J. Alloys Compd.* **2013**, *553*, 216–220.

18. Braic, V.; Vladescu, A.; Balaceanu, M.; Luculescu, C.R.; Braic, M. Nanostructured multi-element (TiZrNbHfTa)N and (TiZrNbHfTa)C hard coatings. *Surf. Coat. Technol.* **2012**, *211*, 117–121.

19. Li, C.J.; Sun, B. Microstructure and property of Al_2O_3 coating microplasma-sprayed using a novel hollow cathode torch. *Mater. Lett.* **2004**, *58*, 179–183.

20. Pan, Q.Y.; Lin, X.; Huang, W.D.; Li, Y.M.; Zhou, Y.H. Microstructure evolution of Cu-Mn alloy under laser rapid solidification condition-Banded structure and planar front growth. *Prog. Nat. Sci.* **1998**, *8*, 79–86.

21. Arnberg, L.; Mathiesen, R.H. Imaging of aluminium alloy solidification by synchrotron X radiation. *Mater. Forum* **2004**, *28*, 47–52.

22. Melo, M.L.N.M.; Rizzo, E.M.S.; Santos, R.G. Numerical model to predict the position, amount and size of microporosity formation in Al-Cu alloys by dissolved gas and solidification shrinkage. *Mat. Sci. Eng. A-Struct.* **2004**, *374*, 351–361.

23. Hunziker, O. Theory of plane front and dendritic growth in multicomponent alloys. *Acta Mater.* **2001**, *49*, 4191–4203.

24. Kurz, W.; Fisher, D.J. *Fundamentals of Solidification*, 4th ed.; Trans Tech Publications: Stafa-Zurich, Switzerland, 1998; p. 83.

25. Lima, M.S.F.; Goldenstein, H. Morphological instability of the austenite growth front in a laser remelted iron-carbon-silicon alloy. *J. Cryst. Growth* **2000**, *208*, 709–716.

26. Steen, W.M.; Mazumder, J. *Laser Material Processing*, 4th ed.; Springer-Verlag London Limited: London, UK, 2010; pp. 317–318.

27. Saunders, N.; Fahrmann, M.; Small, C.J. The application of CALPHAD calculations to Ni-based superalloys. In *Superalloys 2000*; Pollock, T.M., Kissinger, R.D., Bowman, R.R., Green, K.A., McLean, M., Olson, S.L., Schirra, J.J., Eds.; Minerals, Metals & Materials Society: Warrendale, PA, USA, 2000; pp. 803–811.

28. Lin, X.; Yue, T.M.; Yang, H.O.; Huang, W.D. Laser rapid forming of SS316L/Rene88DT graded material. *Mat. Sci. Eng. A-Struct.* **2005**, *391*, 325–336.

29. Kurz, W.; Giovanola, B.; Trivedi, R. Theory of microstructural development during rapid solidification. *Acta Metall.* **1986**, *34*, 823–830.

30. Hunt, J.D. Steady-state columnar and equiaxed growth of dendrites and eutectic. *Mater. Sci. Eng.* **1984**, *65*, 75–83.

31. Gäumann, M.; Trivedi, R.; Kurz, W. Nucleation ahead of the advancing interface in directional solidification. *Mater. Sci. Eng. A* **1997**, *226*, 763–769.

32. Lipton, J.; Kurz, W.; Trivedi, R. Rapid dendrite growth in undercooled alloys. *Acta Metall.* **1987**, *35*, 957–964.

33. Porter, D.A.; Easterling, K.E. *Phase Transformations in Metals and Alloys*; Van Nostrand Reinhold Company: New York, NY, USA, 1981; p. 290.